(2)

FTD-ID(RS)T-1023-89

FOREIGN TECHNOLOGY DIVISION

ADAPTIVE OPTICS CORRECTION IN REAL-TIME FOR DYNAMIC WAVEFRONT ERRORS

by

Jiang Wenhan

Approved for public release;
Distribution unlimited.

HUMAN TRANSLATION

FTD-ID(RS)T-1023-89 15 March 1990

MICROFICHE NR: FTD-90-C-000272

ADAPTIVE OPTICS CORRECTION IN REAL-TIME FOR DYNAMIC WAVEFRONT ERRORS

By: Jiang Wenhan

English pages: 10

Source: Guangxue Xuebao, Vol. 8, Nr. 5, May, 1988, pp. 441-447

Country of origin: China
Translated by: Leo Kanner Associates
F33657-88-D-2188
Requester: FTD/TQTD/Jacobsen

PREPARED BY:

TRANSLATION DIVISION
FOREIGN TECHNOLOGY DIVISION
WPAFB, OHIO.

GRAPHICS DISCLAIMER

All figures, graphics, tables, equations, etc. merged into this translation were extracted from the best quality copy available.

ADAPTIVE OPTICS CORRECTION IN REAL-TIME FOR DYNAMIC WAVEFRONT ERRORS

Jiang Wenhan
Institute of Optics and Electronics, Academia Sinica, Chengdu
Received 3 October 1986; revised 29 December 1986

ABSTRACT

This paper reports on the principles for the use of, and the experimental results obtained from, an adaptive optics system for correcting dynamic wavefront errors in real time. The system consists of a 21-element deformable mirror, a lateral shearing interferometer, and a parallel electronic control system. Key words: Adaptive optics, wavefront sensing, deformable mirror; Chinese Translations

1. FOREWORD

The performance of optical apparatus, in addition to being diminished by static wavefront error produced by the design, machining, installation and adjustment of the apparatus, is also often affected by dynamic wavefront error from deformations arising randomly. For example, atmospheric turbulence affects optical imaging systems and laser transmissions; changes in conditions like temperature and gravity affect the mirrors and bearing structures of large-scale optical equipment, causing deformation and detuning; unevenness of the medium in a laser resonant cavity induc.. lowering in the quality of the beams; and turbulence and heat disturbances d..ng strong laser transmissions in the atmosphere may affect the formation of beam emanations. Traditional optical technology is powerless in the face of these problems.

With the appearance and development of the technology of adaptive optics, the real-time correction of dynamic optical wavefront error has become a possibility [1,2]. Adaptive optical systems measure in real time the wavefront error, and correction of the error in real time is undertaken by the control circuit feedback control wavefront correcting device. If for example the diameter of the wavefront detection and correction subaperture is smaller

than the coherence dimension of the wave front turbulent motion, if the system's control bandwidth is larger than the turbulent motion changing frequency, it is possible to achieve real-time correction of the dynamic wavefront. In the laboratory, we used adaptive optics technology to undertake 21-element-control real-time optical wavefront error correction experiments. Our purpose was to test in the laboratory the correction of atmospheric turbulence and other dynamic factors on wavefront errors occurring in telescope systems, making the telescopes' observation power of resolution approach the technology required for diffraction limit. We shall now report on the principles behind the system and the results of our experiments.

2. EXPERIMENTAL EQUIPMENT AND PRINCIPLES

The principle of a diffraction-limited telescope that is able to correct dynamic wavefront errors is shown in Fig. 1.

The optical system used for our experiments is as shown in Fig. 2. The laser beam emitted by the He-Ne laser, after enlargement, filtering and collimation, passing through a deformable mirror, is divided into three paths. Two of these paths are the x direction and y direction wavefront error detection optical paths, and the third path is used for image quality testing.

A. The Deformable Mirror

The deformable mirror used for this experiment is a composite-style piezoelectric deformable mirror. It features high frequency response, a high degree of sensitivity, a large amount of deformation, and a small time lag. The deformable mirror has 21 actuators used for wavefront error detection; the interval between each two actuators determines the size of the wavefront detector subaperture diameter. The 21 actuators separate the light opening into 16 subapertures along the x and y directions respectively. The small circles with numbers in Fig. 3 represent the actuators, while x_1 through x_{16} are the detector subapertures along the x direction and y_1 through y_{16} are the detector subapertures along the y direction. Different control voltage is

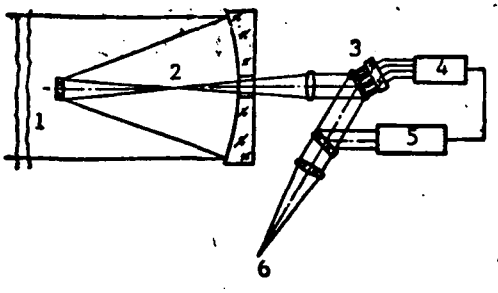

Fig. 1 Schematic layout of the diffraction-limited telescope

1—atmospheric turbulence; *2*—uncorrected image; *3*—deformable mirror; *4*—controller; *5*—wavefront error detector; *6*—corrected image

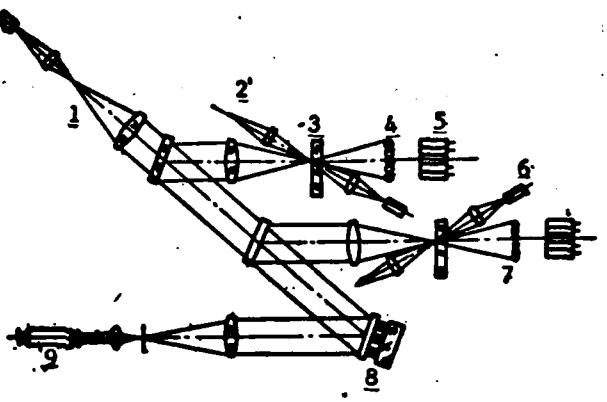

Fig. 2 Optical layout used in experiments

1—image-quality checking optics; *2*—reference optical path; *3*—grating; *4*—lens; *5*—detector array; *6*—*y* direction detecting optical path; *7*—*x* direction detecting optical path; *8*—deformable mirror; *9*—laser

applied on each of the actuators; this allows for controllable change in the shape of the surface of the membrane lenses that are affixed to the actuators, achieving wave front compensation. The entire deformable mirror is activated by two additional actuators; they can automatically produce biaxial inclination and implement inclination correction for the entire device. The light aperture diameter of the deformable mirror is 50 mm, the maximum deformation is ±8μm, the range for the working voltage is ±700 V, and the resonant frequency >7kHz.

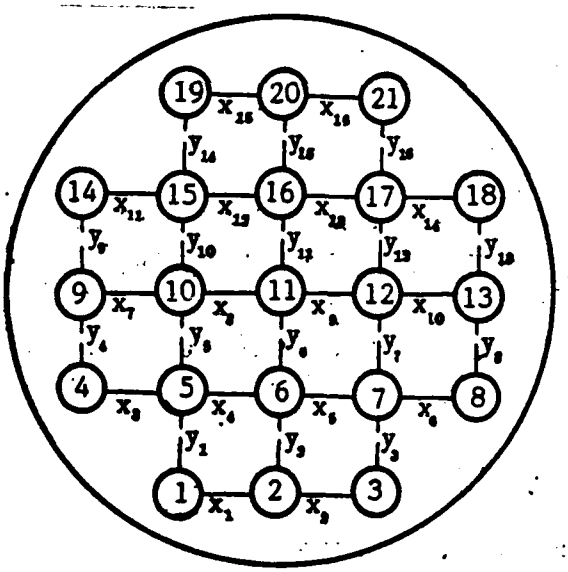

Fig. 3 Arrangement of the actuators of deformable mirror and the subapertures of wavefront sensor

2. DETECTION OF WAVEFRONT ERROR

We used an alternating lateral shearing interferometer (as shown in Fig. 4) to detect dynamic wavefront error [3,4]. Here, the Ranchi grating has two important effects:

1) The wavefront lateral shearing produced by the diffraction effect, forming a self-referring interferometer.

2) While the grating is rotating, it produces signal modulation. The phase angle of the signals shows the wavefront slope.

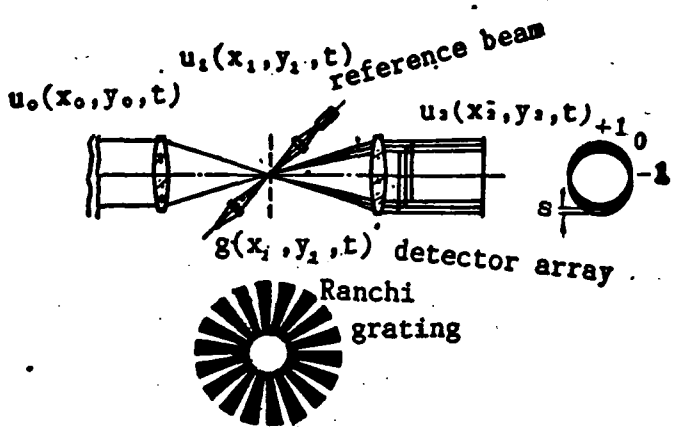

Fig. 4 Shearing interferometer

This is borne out by the fact that the base frequency in the modulated signal of the interferometer of the wavefront $W(w,y)$ shearing in the x direction is:

$$I(w,y,t)=\frac{2}{w}\cos\left[\frac{\pi s^2}{\lambda}\frac{\partial^2 W}{\partial w^2}\right]\cos\left[\omega t+\frac{2\pi}{\lambda}s\frac{\partial W}{\partial w}\right] \tag{1}$$

In the formula, the modulation frequency

$$\omega=2\pi v/p \tag{2}$$

x and y are the coordinates on the aperture surface; v is the linear velocity of the grating rotation; and p is the grating etched line cycle. The phase angle

$$\theta=\frac{2\pi}{\lambda}s\frac{\partial W}{\partial w} \tag{3}$$

and s is the amount of wavefront shearing.

The photoelectric receiver in the detector array must correspond with the subaperture position to be measured, as shown in Fig. 3.

In order to extract the wavefront phase difference signal, another ray of stable light is used in the shearing interferometer as a reference light path, and to provide a reference signal for the electric relative phase. Through phase relation, the phase angle θ is obtained, representing the average wavefront slope within the range of that detector aperture, and from this is obtained the wavefront error ϕ of the adjacent subaperture diameter interval:

$$\phi = \frac{\lambda \theta d_i}{2\pi s}, \tag{4}$$

In the formula, d_i is the size of subaperture θ.

3. Electronic Control System

A block diagram of the electronic control system is provided in Fig. 5.

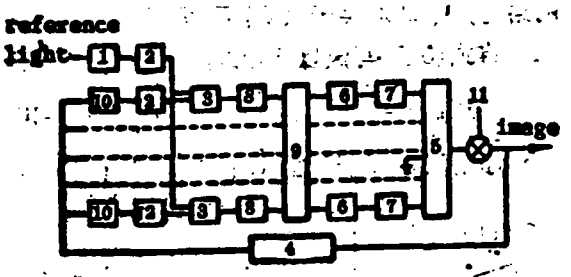

Fig. 5 Block diagram of the electronical control system

1—signal detector; *2*—signal processor; *3*—phase detection; *4*—sharing interferometer; *5*—deformable mirror; *6*—correction network; *7*—high voltage amplifier; *8*—low pass filter; *9*—wavefront reconstruction network; *10*—wavefront slope detector; *11*—analog turbulence signal

The signal received by the photometric circuit and the reference beam circuit receiver, after appropriate processing, undergoes demodulation by the multiplying unit. Because the wavefront average slope or wavefront error within the subaperture is what the shearing interferometer detects, this must be converted by the wavefront reconstruction device into a wavefront value before correction of the detected wavefront can be undertaken. Wavefront restructuring calculation can be performed by a computer or by an analog network. The analog network features simplicity and speed, and for this reason we used the analog network to calculate the wavefront values. The underlying principle is summarized briefly below.

Assume the wavefront corresponding to each actuator of the deformable mirror is W, and that the adjacent actuator wavefront error is ϕ. As regards the NxN actuator array, there are N^2 wavefront values W and $2N(N-1)$ phase errors ϕ. With point (j,k) on Fig. 6(a) as an example, we have:

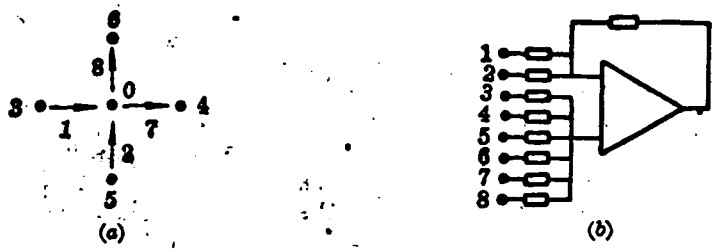

Fig. 6 Principle schema of the wavefront reconstruction analogue network

0—$W_{j,k}$; 1—$\phi_{j-1,k}$; 2—$\phi_{j,k-1}$; 3—$W_{j-1,k}$; 4—$W_{j+1,k}$; 5—$W_{j,k-1}$; 6—$W_{j,k+1}$; 7—$\phi_{j+1,k}$; 8—$\phi_{j,k+1}$

$$\left.\begin{aligned}\phi_{j-1,k}&=W_{j-1,k}-W_{j,k},\\ \phi_{j+1,k}&=W_{j,k}-W_{j+1,k},\\ \phi_{j,k-1}&=W_{j,k-1}-W_{j,k},\\ \phi_{j,k+1}&=W_{j,k}-W_{j,k+1}.\end{aligned}\right\} \tag{5}$$

Obviously, $2N(N-1)>N^2$, so at a minimum it is possible to use multiplication by two to resolve the contradictory set of equations. The normalized set of equations from this contradictory set of equations has the following form:

$$4W_{j,k}-W_{j-1,k}-W_{j+1,k}-W_{j,k-1}-W_{j,k+1}=-\phi_{j-1,k}-\phi_{j,k-1}+\phi_{j+1,k}+\phi_{j,k+1}. \tag{6}$$

Using a matrix form, we can show this as:

$$AW=B\phi, \tag{7}$$

Solving, we obtain:

$$W=A^{-1}B\phi. \tag{8}$$

In the formula, A is the coefficient matrix of wavefront W, A^{-1} is its transposed matrix, and B is the coefficient matrix of phase error ϕ. When an analog network is used, A and B are determined by the structure of the detection array.

We can write formula (5) as follows:

$$W_{j,k}=\frac{1}{4}[W_{j,k-1}+W_{j,k+1}+W_{j-1,k}+W_{j+1,k}+\phi_{j+1,k}+\phi_{j,k+1}-\phi_{j-1,k}-\phi_{j,k-1}]. \tag{9}$$

As shown in Fig. 6(b), the network formed of the elements is able, on the basis of the input phase error ϕ to calculate wavefront W; the calculation units are from considering as input quantities $W_{j,k-1}$, $W_{j,k+1}$, $W_{j-1,k}$, $\phi_{j+1,k}$, $\phi_{j-1,k}$ $\phi_{j,k-1}$ (these quantities coming from the calculated circuit of the other points), and $\phi_{j,k+1}$, $\phi_{j+1,k}$, $\phi_{j-1,k}$, $\phi_{j,k-1}$ (these quantities coming from the output of the phase demodulator). The amplification coefficient is 1/4 the total error amplifier calculation circuit structure.

In order to compensate for the frequency range being an atmospheric turbulence effect from several dozen to over 100 Hz, each circuit in the 21 circuit parallel control system must have a corresponding control bandwidth. For this, we added an amplifying and correcting link. The control system's open-loop frequency characteristics are as shown in Fig. 7.

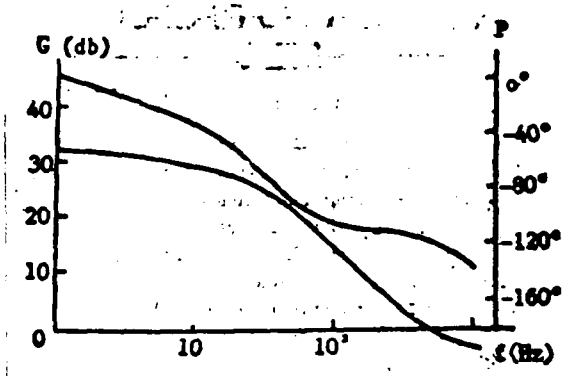

Fig. 7 Open-loop frequency response of the control system

4. Image Quality Checking

We used television to measure the picture elements before and after the dynamic wavefront error correction. After processing the television video frequency signal, we obtained a three dimensional image of the picture element energy distribution; and again using the television image signal digital acquisition system and the computer we analyzed and processed the picture element energy distribution before and after wavefront error correction.

3. EXPERIMENTAL RESULTS

On the actuators of the deformable mirror, after the addition of analog atmospheric turbulence interference signals, the wavefront dynamic error lowered the picture element quality and caused the light energy on the image plane to disperse. Figure 8 shows the experimentally measured results for the

energy profile at the image plane with the perturbation amplitude at $\pm 1\lambda$ and $\pm 2\lambda$.

At the same time that different frequency interference was introduced, the adaptive optical system was turned on to undertake close-loop control; the wavefront error was corrected. Figure 9 shows the experimentally measured results for the energy profile at the image plane after adaptive optical system correction at a frequency of 50 Hz and perturbation amplitudes of $\pm 1\lambda$ and $\pm 2\lambda$.

(a) (b)

Fig. 8 The energy profile at image plane with perturbation, open-looped, amplitude (a) $\pm 1\lambda$; (b) $\pm 2\lambda$

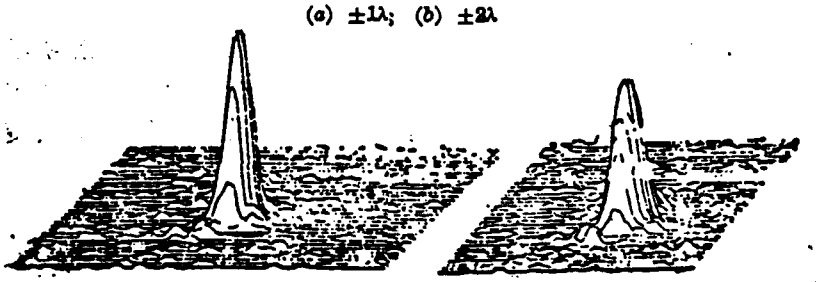

(a) (b)

Fig. 9 The energy profile at image plane with perturbation, close-looped, frequency 50Hz (a) $\pm 1\lambda$; (b) $\pm 2\lambda$

We undertook computer data acquisition and analysis on the experimental energy profiles, and calculated the proportion of the total energy represented by the light energy in the circles of different dimensions on the image spots. We obtained an integral graph of the image plane energy distribution. Figure 10 shows the integral energy graph with a wavefront perturbation of 100 Hz and an amplitude of ±1 after correction. On the graph, the units of the horizontal coordinate are the diameter $D=2.44\lambda f/d$ of the Airy spot first dark circle. d and f are respectively the optical system aperture and the focal

distance. The vertical coordinate is the percentage of light energy in the circle of that diameter.

When introducing different frequency perturbation (range value $\pm 1\lambda$), we measured the percentage of energy within the Airy spot first dark circle, as shown in Table 1. With a diffraction limit, the energy inside the Airy spot represented 83.8% of the total. On the table, the ratio between the experimentally measured values and the theoretical diffraction limits is also displayed.

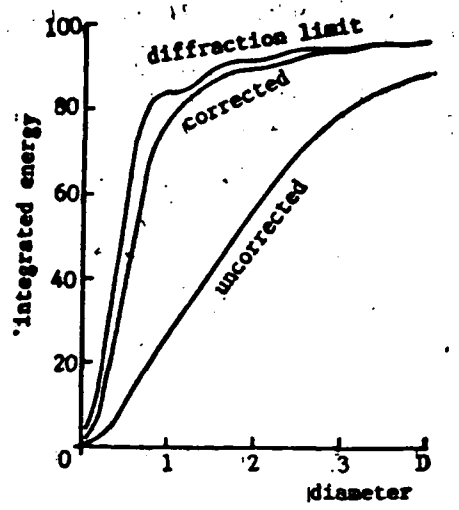

Fig. 10 Comparison of the integral energy at image plane with/without perturbation and diffraction limit

Table 1 Energy of image spot with $D=2.44\frac{\lambda}{d}f$

perturbation frequency	without correction		with correction	
	measured value	measured value/ diffraction limit	measured value	measured value/ diffraction limit
50 Hz	26%	31%	80%	96%
100 Hz			78%	93.5%
300 Hz			60%	71%

From this it can be seen that, after correction by the adapting optical system, the degree of energy concentration shows a very great increase, approaching the ideal diffraction limit.

In addition, we used the frequency response analyzer to measure, for an analog signals with an amplitude of one wave length and a frequency of 1 Hz, 10 Hz, 100 Hz and 300 Hz, the wavefront error correction capability; the results were respectively -35, -33, -17, -10, and -6 dB.

4. CONCLUSIONS

After constructing a 21-element adapting optical system and undertaking wavefront error correction experiments, we have shown that the system is able to perform correction for dynamic wave front errors in round apertures for 300 Hz and less; and that the error correction results are immediately apparent. The principles of detection of surface dynamic wavefront error and the wavefront restoration analog computation network are correct. The bandwidth of the control system is sufficient, and the working of the 21-element deformable mirror is normal.

Among the main persons involved in the development of the experimental apparatus and the implementation of the experiments are Li Mingquan, Wang Wenming, Yan Peiying, Dai Zichang, and Hao Peiming. Ling Ning and Yu Beiwen provided the deformable mirror. Rong Zhijun, Li Mei, and Xiao Shijiang, among others, undertook the work of computer data acquisition and processing. In addition, we were assisted by very many other colleagues. This work was funded by the Chinese Academy of Science. At this time, we wish to thank them all.

REFERENCES

1. Hardy, J.W. Proc. IEEE, 1978, 66, No. 6 (Jun), 651-679.

2. Pearson, J.E. et al. Appl. Opt. and Opt. Eng., 7 (edited by R.R. Shannon and J.C. Wyant, Academic Press, New York, 1979), 245-340.

3. Koliopoulos, C.L. Appl. Opt., 1980, 19, No. 9 (May), 1523-1528.

4. Southwell, W.H. J.O.S.A., 1980, 70, No. 8 (Aug), 998-1005.

DISTRIBUTION LIST

DISTRIBUTION DIRECT TO RECIPIENT

ORGANIZATION	MICROFICHE
C509 BALLISTIC RES LAB	1
C510 R&T LABS/AVEADCOM	1
C513 ARRADCOM	1
C535 AVRADCOM/TSARCOM	1
C539 TRASANA	1
C591 FSTC	4
C619 MIA REDSTONE	1
D008 MISC	1
E053 HQ USAF/INET	1
E404 AEDC/DOF	1
E408 AFWL	1
E410 AD/IND	1
F429 SD/IND	1
P005 DOE/ISA/DDI	1
P050 CIA/OCR/ADD/SD	2
AFIT/LDE	1
NOIC/OIC-9	1
CCV	1
MIA/PHS	1
LLYL/CODE L-309	1
NASA/NST-44	1
NSA/T513/TDL	2
ASD/FTD/TTIA	1
FSL	1